ADVANCED MATERIALS
www.advmat.de

Phase-Change Perovskite Microlaser with Tunable Polarization Vortex

*Jingyi Tian, Giorgio Adamo, Hailong Liu, Mengfei Wu, Maciej Klein, Jie Deng, Norman Soo Seng Ang, Ramón Paniagua-Domínguez, Hong Liu, Arseniy I. Kuznetsov, and Cesare Soci**

Metasurfaces supporting optical bound states in the continuum (BICs) are emerging as simple and compact optical cavities to realize polarization-vortex lasers. The winding of the polarization around the singularity defines topological charges which are generally set by the cavity design and cannot be altered without changing geometrical parameters. Here, a subwavelength-thin phase-change halide perovskite BIC metasurface functioning as a tunable polarization vortex microlaser is demonstrated. Upon the perovskite structural phase transitions, both its refractive index and gain vary substantially, inducing reversible and bistable switching between distinct polarization vortexes underpinned by opposite topological charges. Dynamic tuning and switching of the resulting vector beams may find use in microscopy imaging, particle trapping and manipulation, and optical data storage.

1. Introduction

Optical bound states in the continuum (BICs), which are perfectly confined optical modes located in the continuum spectrum of free-space radiation, have proven to be a powerful tool for suppressing radiative losses, allowing the realization of extremely compact lasing cavities with ultra-high Q-factors and low lasing thresholds.[1–5] BICs are vortex centers in the far-field polarization that carry quantized topological invariants (i.e., topological charge) corresponding to the winding of the polarization vectors. Typically, the light outcoupled via BICs, in emission or transmission, is a polarization vortex beam whose topological invariant is set by the cavity design and cannot be altered without changing its geometrical parameters. Recent realizations of BIC modulation via electrical, optical, or acoustical signals have been limited to on-off state switching or wavelength tuning of the state. [1,6–11] Dynamic switching between BICs with different topological charges, a degree of freedom not yet unlocked, would offer new opportunities for switchable metasurfaces, integrated active nanophotonic devices, and tunable vector beams.

Functional metasurfaces relying on phase-change media like chalcogenides,[10–14] metal-oxides,[15] and liquid crystals[9,16] offer solutions for dynamically tunable devices in a compact footprint.[17] However, while conventional phase-change media are widely exploited in passive reflective and transmissive devices, they are not suitable for active light emitting devices like lasers, due to the lack of optical gain. Thus, identifying a class of phase-change materials with tunable refractive index and optical gain could truly transform the landscape of active topological devices.

Halide perovskites are an emerging class of photonic materials that combine, in a single platform, excellent luminescence properties and high refractive index. This has allowed realization of efficient light emitting devices[18,19] and dielectric nanophotonic structures[20] such as high-resolution color displays, [21,22] photoluminescence (PL)-enhanced metasurfaces, [23] and low-threshold lasers.[1,24] In addition, due to the strong interplay between inorganic framework and organic ligands, halide perovskites display a rich variety of crystallographic phases which depend on chemical composition,[25] pressure,[26] and temperature.[27] Transitions between these phases are often associated with a large variation of the refractive index and the emission characteristics. [27–30]

In this work, we demonstrate dynamic switching of topological charges in a BIC microlaser using a subwavelength-thin halide perovskite metasurface that acts concurrently as phase-change tunable gain medium and high-quality factor cavity. The cavity design is based on a dielectric metasurface embossed in the perovskite that supports optical BICs,[2–5,31] giving a highly directional polarization-vortex emission. The variation in optical constants and luminescence upon phase transition

J. Tian, G. Adamo, M. Klein, C. Soci
Centre for Disruptive Photonic Technologies
TPI
Nanyang Technological University
21 Nanyang Link, Singapore 637371, Singapore
E-mail: csoci@ntu.edu.sg
J. Tian, G. Adamo, M. Klein, C. Soci
Division of Physics and Applied Physics
School of Physical and Mathematical Sciences
Nanyang Technological University
21 Nanyang Link, Singapore 637371, Singapore
H. Liu, M. Wu, J. Deng, N. S. S. Ang, R. Paniagua-Domínguez, H. Liu, A. I. Kuznetsov
Institute of Materials Research and Engineering
A*STAR (Agency for Science Technology and Research)
2 Fusionopolis Way, #08-03, Innovis, Singapore 138634, Singapore
The ORCID identification number(s) for the author(s) of this article can be found under https://doi.org/10.1002/adma.202207430.

DOI: 10.1002/adma.202207430

results in deterministic switching between two different BICs, which enables spatial tunability of the laser emission profile between polarization vortexes carrying opposite topological charges at different wavelengths. At the same time, the thermal modulation of spatial and spectral characteristics shows hysteresis-induced optical bistability. These findings demonstrate the potential of phase-change halide perovskites for the generation of tunable vector beams, which may find application in microscopy imaging,[32] particle trapping and manipulation, [33] and optical data storage.[34,35]

2. Results and Discussion

2.1. Design of a Phase-Change Perovskite BIC Metasurface

To support BICs, the metasurface design must possess in-plane inversion symmetry (C_2 symmetry). Here, we use a square lattice of circular holes, which supports multiple BICs in the spectral region of interest. Because of their theoretically infinite quality factor, BICs correspond to zero-intensity regions in the far field. They will therefore appear as singularity points of far-field polarization vectors in the momentum space and carry conserved and quantized topological charges as vortex centers. The topological charge (i.e., topological winding number), q, carried by BICs is defined as[4]

$$q = \frac{1}{2\pi}\oint_C dk \cdot \nabla_k \varphi(k), q \in Z \quad (1)$$

where $\varphi(k)$ is the angle between the polarization vector and the x-axis and C denotes a counterclockwise closed loop around the BICs in momentum space. Accordingly, q indicates how many times the polarization vector winds around the BICs and must therefore be an integer.

For the demonstration of the phase-change perovskite BIC metasurface, we select a prototypical halide perovskite, methylammonium lead iodide $CH_3NH_3PbI_3$ ($MAPbI_3$). $MAPbI_3$ has proven to be a dependable high refractive index platform for all-dielectric perovskite metasurfaces and exhibits a tetragonal-orthorhombic structural phase transition at 130–160 K,[27,28] associated with considerable modification in refractive index and gain spectrum (see Figures S1–S3, Supporting Information I and II). The phase-change figure of merit of $MAPbI_3$, $FOM = |\Delta n|/(k_1 + k_2) = 0.78$ at 790 nm (Δn is the change of refractive index and $k_1 + k_2$ the sum of extinction coefficients of the two phases) is higher than the prototypical phase-change chalcogenide material $Ge_2Sb_2Te_5$ with FOM ≈0.2 at the same wavelength . [36]

The BIC metasurface is patterned in a 250 nm thick $MAPbI_3$ film, sandwiched between a thick polydimethylsiloxane (PDMS) layer and a quartz substrate (**Figure 1**). The metasurface is designed to support two high-Q BICs within the optical gain region above the absorption edge of $MAPbI_3$ (>750 nm)—an out-of-plane (x–y plane) magnetic dipole mode (MDz-BIC) and a magnetic quadrupole mode (MQ-BIC). Under optical excitation, the perovskite microlaser will selectively emit a highly collimated polarization vortex beam in the near-IR, underpinned by either one of the BIC modes of the metasurface. Upon temperature change, the $MAPbI_3$ perovskite adopts two distinct crystal structures, that is, the room-temperature tetragonal phase and the low-temperature orthorhombic phase, and the polarization vortex will switch its topological charge between +1 and −1 (Figure 1).

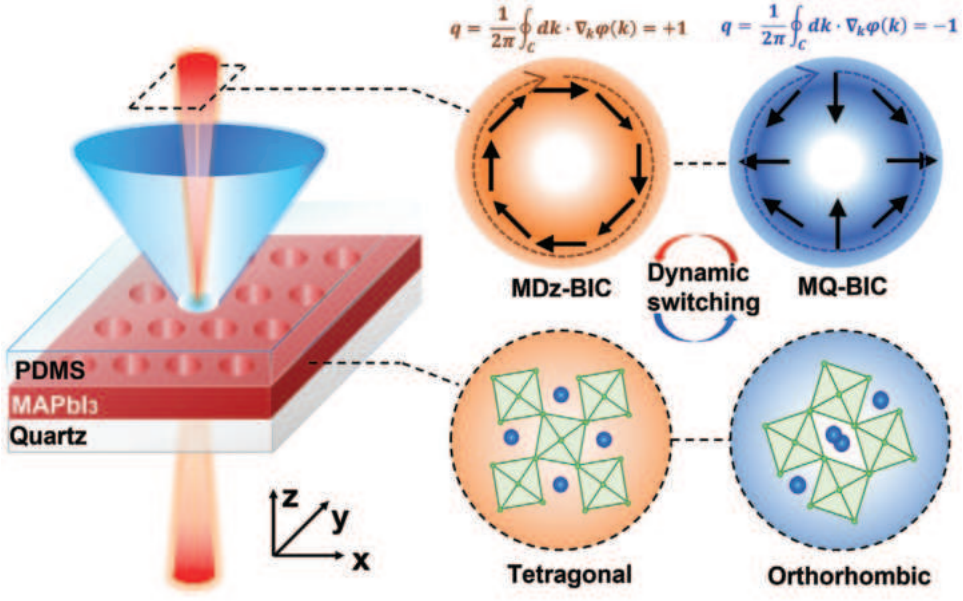

Figure 1. Phase-change perovskite microlaser with tunable topological polarization singularity. Schematic of the tunable microlaser based on a phase-change perovskite BIC metasurface. The perovskite is sandwiched between two $n = 1.5$ layers (quartz and PDMS), pumped with blue laser ($\lambda = 405$ nm), and emits a highly collimated polarization vortex beam in the near-IR. The polarization of the vortex can be dynamically switched between two different BICs carrying opposite topological charges, by driving the $MAPbI_3$ across its phase transition, between the room-temperature tetragonal phase and the low-temperature orthorhombic phase.

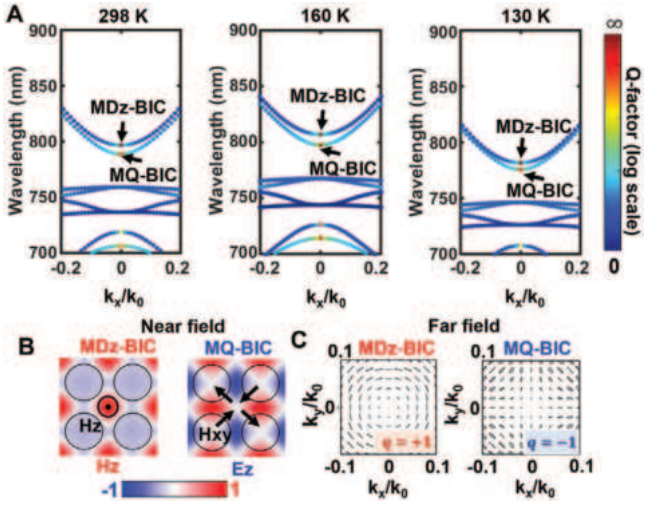

Figure 2. BICs of the phase-change metasurface at different temperatures. A) Calculated band structures of the $MAPbI_3$ metasurface within the optical gain spectral region, at 298 K (tetragonal phase), 160 K, (tetragonal phase), and 130 K (orthorhombic phase). The color map indicates the radiative quality factors of the modes: two BICs (i.e., MDz-BIC and MQ-BIC) appear near $k = 0$ for $\lambda > 750$ nm with divergent Q-factors (highlighted by the black arrows). B) Calculated near-field H_z and E_z field distribution of the two BICs in the x–y plane, with antinodes confined within the perovskites film. C) Far-field polarization maps near the MDz-BIC and MQ-BIC in the momentum space; the rotation of the main axis of polarization across a counterclockwise loop results in polarization topological charges of opposite value, +1 and -1, respectively.

2.2. Tuning of BICs Induced by the Perovskite Structural Phase Transition

The optical band diagrams in **Figure 2**a show the dispersion of the MDz and MQ high-Q modes supported by the metasurface. The modes give rise to symmetry-protected BICs (MDz-BIC and MQ-BIC) at $k_x = 0$, appearing as singularity point at the center of far-field polarization vortexes. The Q factors of both MDz and MQ modes of the metasurface diverge to infinity near $k_x = 0$, (indicated by the red dots and black arrows in Figure 2a). By controlling the ambient temperature, the two BICs can be sustained and tuned across the $MAPbI_3$ structural phase transition. As the temperature decreases from 298 to 160 K, the change of refractive index induces a large shift of the spectral position of MDz-BIC (MQ-BIC), from 797 to 806 nm (789 to 797.5 nm); when the temperature is further reduced to 130 K, the spectral position of MDz-BIC (MQ-BIC) shifts back to 782 nm (776 nm). Throughout these regions, the electromagnetic fields of both MDz-BIC and MQ-BIC remain mostly confined within the perovskite film, guaranteeing optimal spatial mode-gain overlap (Figure 2b).

The calculated far-field polarization maps, projected by the BICs in the momentum space (Figure 2c), clearly show that, when following a counterclockwise closed loop around $k = 0$, the main axis of polarization (black lines) winds counterclockwise for MDz-BIC and clockwise for MQ-BIC. Based on the definition of BIC topological charges expressed by Equation (1), MDz-BIC and MQ-BIC correspond to TE and TM polarization vortexes in the k-space with topological charges of +1 and –1, respectively.

The $MAPbI_3$ metasurface is fabricated by nanoimprint lithography (NIL) (see Experimental Section). The circular holes, with a diameter of 300 nm, are arranged in a square lattice with 400 nm period and imprinted to a depth of ≈200 nm within the 250 nm thick film, as shown in **Figure 3**a. Besides large area nanostructuring, NIL provides additional advantages such as improvement of surface morphology (Figure S4, Supporting information III) and increase of environmental stability of the perovskite film.[37]

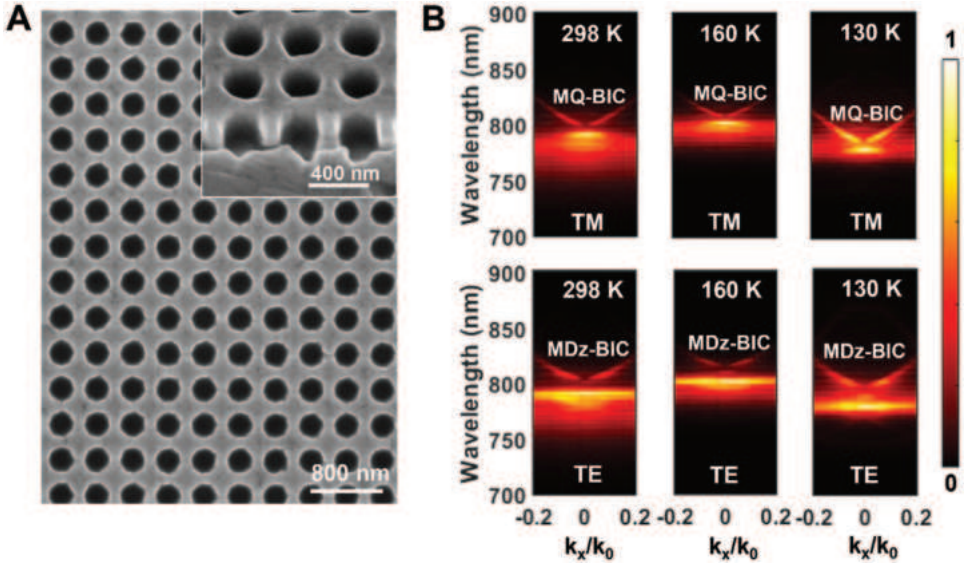

Figure 3. A) SEM image of a $MAPbI_3$ film patterned with a square lattice of circular holes by nanoimprint lithography. The inset shows the cross section of the perovskite metasurface. B) Experimental TM-polarized and TE-polarized angle-resolved photoluminescence maps (PL) at 298 K (tetragonal phase), 160 K (tetragonal phase), and 130 K (orthorhombic phase), under 405 nm continuous wave (CW) laser excitation, showing temperature-tunable, distinct MQ-BIC and MDz-BIC dispersion bands of vanishing intensity at $k_x = 0$.

Since both BICs are located within the emission region of $MAPbI_3$, its photoluminescence is expected to efficiently couple to these optical modes with angular emission pattern closely resembling the optical bands in Figure 2a. Angle-resolved PL is measured at three representative temperatures for transverse magnetic (TM) and transverse electric (TE) polarizations, and the corresponding spectral maps are shown in Figure 3b. The BIC nature of the MQ mode (TM-polarized) and MDz mode (TE-polarized) is revealed by the PL bands with vanishing emission linewidth near the normal direction ($k_x = 0$) while resonances disappear in the absorption region above the $MAPbI_3$ band edge. As predicted by the simulations in Figure 2a, the PL bands redshift when the temperature decreases from 298 to 160 K, and rapidly blueshift when the temperature decreases further to 130 K.

2.3. Polarization Vortexes in Phase-Change Perovskite BIC Microlaser

Lasing from the BIC metasurface is characterized under frequency-doubled fs-laser pump (λ = 400 nm), with 100 fs pulse duration and 1 kHz repetition rate. The pump-fluence dependence of the room temperature emission spectra is shown in **Figure 4**a. The broad emission spectrum observed at low pump fluences is overtaken by a single narrow lasing peak (λ = 797 nm) at higher fluences (inset of Figure 4a). The dominant lasing mode at room temperature is the MDz-BIC at λ = 797 nm, while the MQ-BIC is inhibited by the higher absorption of $MAPbI_3$ at shorter wavelengths (Figure S1b, Supporting Information). The onset of lasing at room temperature can be easily identified in the light–light curve, yielding a lasing threshold of 8 μJ cm^{-2}, while concurrently the emission linewidth undergoes a sharp narrowing by two orders of magnitude at the lasing threshold, corresponding to a Q factor of 796 (Figure 4b). Above the lasing threshold, the unpolarized far-field radiation shows the typical donut shape of polarization vortex beams, with diverging angle of ≈1.02°, whereas the polarization-dependent beam profiles confirm the winding of the electric field vector around the singularity point, with the +1 polarization topological charge associated with the MDz-BIC (for the far-field radiation below the threshold, see Figure S6, Supporting Information V).

The lasing mode changes to MQ-BIC at λ = 791 nm (Figure 4d), after $MAPbI_3$ undergoes the phase transition which induces a blue shift in the absorption edge of $MAPbI_3$ (Figure S1b, Supporting Information), resulting in better spectral overlap between the MQ-BIC and the optical gain. Consequently, together with reduced nonradiative channels at low temperature, the lasing threshold reduces to ≈2.2 μJ cm^{-2} at 135 K and the Q factor of the lasing mode increases to 880 (Figure 4e). In this case, far-field imaging of the unpolarized and polarized radiation patterns above the lasing threshold reveals a polarization vortex carrying a −1 topological charge of MQ-BIC with diverging angle about 1.18° (Figure 4f).

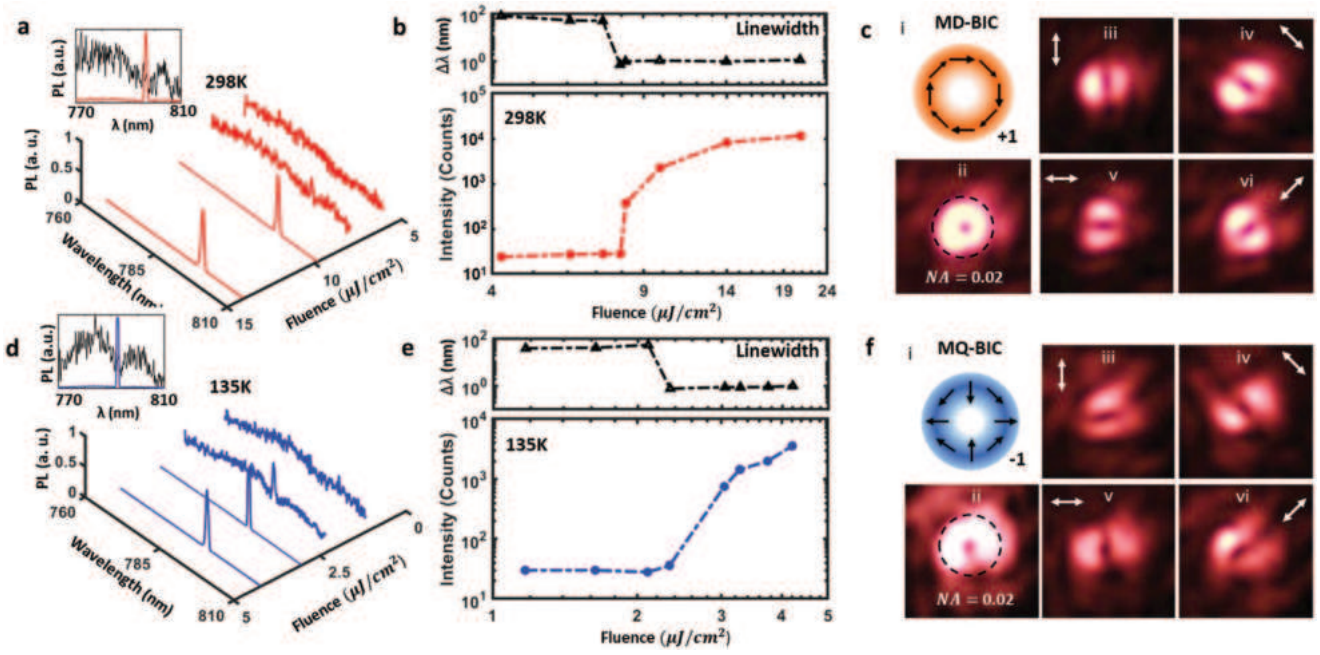

Figure 4. Laser performance of the polarization-vortex microlaser. A) Room-temperature emission spectra of the $MAPbI_3$ BIC metasurface as function of pump fluence. The inset shows the normalized PL spectra below (black curve) and above (red curve) the lasing threshold. B) Emission linewidth (top) and intensity (below) curves for the lasing peak at room-temperature. C) Schematic of a TE-polarized polarization vortex emission with +1 topological charge (i); donut-shaped, room temperature, unpolarized far-field radiation pattern of the metasurface (ii); far-field laser beam profiles passing through a polarizer at four different orientations (iii–vi). D) Emission spectra of the metasurface as function of pump fluence, at 135 K. The inset shows the normalized PL spectra of a $MAPbI_3$ metasurface below (black curve) and above (blue curve) the lasing threshold. E) Emission linewidth (top) and intensity (below) curves for the lasing peak at 135 K. F) Schematic of a TM-polarized vector beam with -1 topological charge (i); unpolarized far-field radiation pattern of the metasurface, at 135 K (ii); far-field laser beam profiles passing through a polarizer at four different orientations (iii–vi).

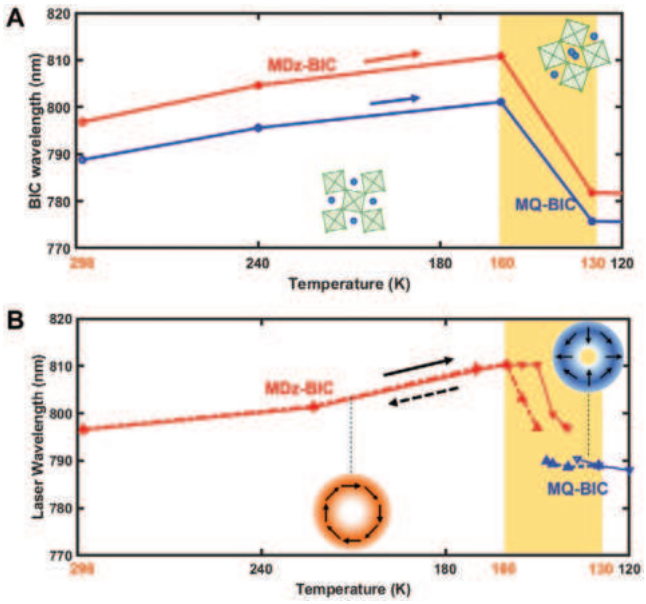

Figure 5. Dynamic switching of the polarization vortexes. A) Calculated wavelength shift of the MDz-BIC (red) and MQ-BIC (blue), as function of temperature, caused by the temperature-induced refractive-index change of the perovskite undergoing tetragonal to orthorhombic phase transition. B) Dynamic mode switching and wavelength shift of the laser emission upon a temperature decrease and increase cycle. Bistability (hysteresis behavior) can be observed in the phase-transition region (130–160 K).

2.4. Dynamic Switching of the Polarization Vortexes

The evolution of the BICs across the 298 and 130 K temperature range is calculated through full-wave Maxwell solver simulations, accounting for the refractive index change of the perovskite. Three distinct regions appear, that is, a high-temperature region with $T > 160$ K, where the perovskite is in the tetragonal phase, an intermediate temperature region with 130 K < T < 160 K, where both tetragonal and orthorhombic phases of the perovskite coexist, and a low temperature region with $T < 130$ K, where the perovskite is in the orthorhombic phase (**Figure 5**a). When the temperature decreases from 298 to 160 K, the two BICs at 797 and 789 nm gradually redshift by more than 10 nm, corresponding to a tuning rate of 0.1 nm K^{-1}. Upon entering the intermediate region (yellow band in Figure 5a), the peak positions of the MDz-BIC and MQ-BIC blue shift at much higher rates of –0.97 and –0.85 nm K^{-1}, respectively, and stabilize at 782 and 776 nm when the phase transition is completed.

The evolution of the experimental lasing mode across the same temperature range, for a full cooling and heating cycle, is shown in Figure 5b (refer to Figure S7, Supporting Information, for the spectra). When the perovskite is in the tetragonal phase (160 K< T < 298 K), the metasurface lases in the MDz-BIC mode because of a more favorable mode-gain overlap and the mode can be tuned continuously between 797 and 811 nm at a rate of 0.1 nm K^{-1}. As the perovskite enters the intermediate region (yellow), the sign of the tuning rate is inverted and the laser wavelength moves between 811 and 788 nm at a much higher rate of –1.35 nm K^{-1}. Within the phase transition region, the laser mode changes between MDz-BIC and MQ-BIC due to variation in the mode-gain overlap, and the polarization topological singularity switches from +1 to –1. The metasurface then continues to lase in the MQ-BIC mode when the perovskite is in the orthorhombic phase ($T < 130$ K).

Interestingly, the temperature dependence of the laser emission wavelength does not follow the same path during the cooling and the heating cycles, forming a hysteresis loop. This is underpinned by the hysteresis of the dielectric permittivity of $MAPbI_3$ across the phase transition.[27] Bistable operation of the microlaser is attainable within the hysteresis region when the laser switches between the MDz-BIC and the MQ-BIC. This allows generating two stable polarization vortex beams, with opposite topological charges at the same temperature, which can be addressed within the heating or cooling branches of the temperature hysteresis loop. This is further illustrated in Figure S8, Supporting information VI, where the microlaser undergoes several cooling and heating cycles between 135 and 155 K. The microlaser can be switched repeatedly between the two stable modes, showing good retentivity and spatial and spectral mode reproducibility (a video of the continuous mode switching is also available in Supporting Information).

3. Conclusions

The concept of tunable polarization-vortex microlaser is underpinned by the unique properties of halide perovskites, which combine, in a single platform, crystallographic phase-dependent optical gain/loss and refractive index change—unlike conventional phase-change media that typically lack optical gain. From a fundamental point of view, the interdependence of tunable gain/loss and refractive index has enabled this present realization of a light-emitting metadevice with switchable topological charges, one of the open challenges in topological nanophotonics. Further than that, phase-change perovskites will provide new opportunities for the exploration of dynamically tunable non-Hermitian phenomena, such as reconfigurable parity-time symmetry lasers,[38] phase manipulation via exceptional points,[39] or dirigible non-reciprocal light propagation.[40]

On the other hand, this device concept may find use in applications such as microscopy imaging that could benefit from active control of polarization and wavelength of the light source,[32] particle trapping and manipulation in which the degree of polarization of vector beams (e.g., radial or azimuthal) can lead to distinctive optical forces at the trapping plane,[33] or dense optical data storage relying on polarization multiplexing.[35] Practical implementations would require faster switching speed and higher operating temperatures. Despite the thermal nature of the conversion mechanism, phase-change materials can achieve remarkable switching speed and energy efficiency, as established in phase-change optical and electronic memories.[41] In the perovkite phase-change tunable microlaser, the switching speed between lasing modes and the required energy are related to the activation energy (E_a) of the phase transformation. In $MAPbI_3$, the activation energy of the orthorhombic-to-tetragonal phase transition is only E_a = 245 meV,[42] typical of a structural rearrangement induced by molecular reorientation. This is one order of magnitude lower than the activation energy of conventional phase-change chalcogenides,

such as $Ge_2Sb_2Te_5$, in which E_a = 2–3 eV.[43] Moreover, while the relevant structural phase transition of $MAPbI_3$ occurs at T = 130–160 K, hybrid perovskites with higher transition temperatures are available, for example, $(C_4H_9NH_3)_2PbI_4$ which displays large variation of refractive and emissive properties at T = 240–270 K[29]—a phase-transition temperature range already compatible with thermoelectric cooling.

In summary, we demonstrated a subwavelength-thin phase-change perovskite microlaser with unprecedented combination of reversible and bistable switching of polarization vortexes and spectral tunability. This demonstration expands the toolbox of BIC modulation, recently realized via electrical, optical, or acoustical signals, beyond the on-off state switching. Our work highlights the potential of phase-change perovskites that combine tunable gain/loss and refractive index change for the realization of a new class of wavelength and polarization tunable microlasers and for the exploration of new phenomena in topological and non-Hermitian photonics.

4. Experimental Section

Film Preparation: $MAPbI_3$ thin films were fabricated from a 1.2 M precursor solution of CH_3NH_3I (Dyesol) and PbI_2 (99.99%, TCI) (molar ratio 1:1) in anhydrous dimethylformamide (Sigma-Aldrich). As prepared solution was magnetically stirred overnight at room temperature in a N_2-filled glovebox, then filtered by a polyvinylidene fluoride syringe filter (0.45 µm), and left on the hot plate at 373 K for 1 h before spin-coating. Prior to perovskite deposition, quartz substrates were cleaned by immersing in the following solution: 2 mL of Hellmanex II (Hellma Analytics) in 200 mL of deionized (DI) water at 353 K for 10 min. Subsequently, substrates were rinsed with DI water and dried with the flow of nitrogen followed by oxygen plasma cleaning treatment. The perovskite precursor solution was spin-coated onto the quartz substrates with a speed of 4900 rpm for 30 s using antisolvent engineering method. Toluene was drop-casted on the substrates 5 s after the start of the spin-coating program. The resulting films were finally annealed at 373 K for 15 min.

Master Mold Fabrication: A thickness of 170 nm HSQ (hydrogen silsesquioxane, XR-1541-006) was spin-coated on the Si substrate at 1500 rpm for 60 s. The designed patterns were exposed with an e-beam lithography system (ELS-7000, Elionix) at an acceleration voltage of 100 kV, current of 500 pA, and dose of 7600 µC cm^{-2}. The exposed sample was developed in salty developer (KOH 1%, NaCl 4%, DI water 95%) for 60 s, and rinsed with DI water for 60 s. The Si was etched by inductively coupling plasma (ICP, Oxford plasmalab 100 ICP/DRIE) with a mixture of HBr (50 sccm) and O_2 (3 sccm) gases at 5 mTorr, CP power of 800 W, and RIE power of 150 W. After Si etching, the HSQ mask was removed by soaking the sample in buffered hydrofluoric acid for 5 min and then rinsed with DI water.

Thermal Nanoimprinting: The master mold was coated with silane as an anti-sticking layer. Thermal nanoimprinting process was performed with Obducat NIL-60-SS-UV-Nano-Imprinter at 30 bar and 90 °C. The master mold was put on top of the perovskite film, and covered with plastic sheet as a protection layer. The imprinting time was 30 min, and then the sample was cooled down to 30 °C before the demolding process. The printed sample was manually demolded from the master mold.

Numerical Simulation: The optical bands and quality factor of perovskite metasurfaces were calculated using 3D finite-element method (Comsol Multiphysics 5.4). The unit cell consisted of a square perovskite slab with circular hole at the center, embedded in a homogeneous background (n = 1.5). Floquet periodic boundary conditions were used in the x and y directions while perfectly matched layers were used along the z-direction. The optical bands and the corresponding far-field vector distributions in the momentum space were calculated using the eigen-frequency solver by sweeping the in-plane wavevectors. The optical constants of the $MAPbI_3$ films were based on datasets from ref. [24].

Angle-Resolved Photoluminescence Map: The angle-resolved photoluminescence spectra were measured by back focal plane (BFP) spectroscopy. The sample was placed in a cryostat (Janis Research ST-500), cooled by liquid nitrogen and connected to a temperature controller (Scientific Instruments Model 9700). The sample was positioned at the image plane of an inverted optical microscope (Nikon Ti-U) with a long working distance objective (50×, NA 0.55). The pump beam from a continuous-wave laser at λ = 405 nm was expanded by a lens before exciting the sample through the 50× objective, giving a pump spot diameter of ≈ 30 mm. The PL signal from the sample was collected through the same 50× objective and a long-pass filter, followed by a series of lenses that image the BFP of the objective onto the entrance slit of a spectrometer (Andor SR-303i). The slit was 100 mm in width and was aligned with the x axis of the sample, that is, collecting the emission in the x–z plane. A grating with 150 lines mm^{-1}, blazed at 800 nm dispersed the light past the slit, resulting in an angle- and wavelength-resolved PL map, eventually captured on a 2D EMCCD camera (Andor Newton 971).

Laser Characterization: Photoluminescence of the metasurface was measured by a frequency doubled Ti:Sapphire laser (400 nm, using a BBO crystal) from a regenerative amplifier (repetition rate 1 kHz, pulse width 100 fs, seeded by Mai Tai, Spectra Physics). The pumping laser was focused by a convex lens (with focus length of 3 cm) onto the top surface of the sample, and the spot size on the sample was about 50 µm. Emitted light and corresponding fluorescence microscopy image were collected on the backside of the metasurface by a 5× objective lens coupled with a CCD coupled spectrometer (Acton IsoPlane SCT 320) and a camera, respectively. An attenuator and an energy meter were used to tune and measure the pumping density. For laser characterization under different temperatures, the metasurface was mounted inside a Linkam Stage with temperature controller. The temperature was changed by 5 K min^{-1} and stabilized at each target temperature for 5 min before conducting measurement.

Supporting Information

Supporting Information is available from the Wiley Online Library or from the author.

Acknowledgements

The authors are thankful to Guanghui Yuan for useful discussions and acknowledge the help of Elena Feltri with optimization of the perovskite films, Bera Kanta Lakshmi with development of the nanoimprint lithography process, and Ha Son Tung with angle-resolved photoluminescence measurements. The research was supported by the Agency for Science, Technology and Research A*STAR-AME programmatic grant on Nanoantenna Spatial Light Modulators for Next-Gen Display Technologies (Grant no. A18A7b0058), the Singapore Ministry of Education (Grant no. MOE2016-T3-1-006), National Research Foundation of Singapore (Grant no. NRF-NRFI2017-01), and IET A F Harvey Engineering Research Prize 2016.

Conflict of Interest

The authors declare no conflict of interest.

Author Contributions

J.T. and G.A. contributed equally to this work. C.S., J.T., G.A., R.P.D., and A.I.K. conceived the idea. J.T. performed the numerical simulations and theoretical analysis. J.T. and G.A. developed the setup to test lasing

regime and conducted the laser characterization measurements. J.T., G.A., and C.S. wrote the first draft of the manuscript. M.W. performed the angle-resolved photoluminescence measurement. M.K. synthesized the perovskite film. Hailong L., J.D., and N.S.S.A. performed the nanoimprint lithography process under the supervision of Hong L. All authors contributed to the writing of the manuscript.

Data Availability Statement

The data that support the findings of this study are openly available in NTU at https://doi.org/10.21979/N9/LJ5JVM.

Keywords

all-dielectric metasurfaces, optical bistability, phase-change perovskites, polarization vortices, tunable microlasers, tunable topological charges

Received: August 15, 2022
Revised: October 7, 2022
Published online: November 22, 2022

[1] C. Huang, C. Zhang, S. Xiao, Y. Wang, Y. Fan, Y. Liu, N. Zhang, G. Qu, H. Ji, J. Han, *Science* **2020**, *367*, 1018.
[2] Q. Song, J. Hu, S. Dai, C. Zheng, D. Han, J. Zi, Z. Zhang, C. T. Chan, *Sci. Adv.* **2020**, *6*, eabc1160.
[3] M.-S. Hwang, H.-C. Lee, K.-H. Kim, K.-Y. Jeong, S.-H. Kwon, K. Koshelev, Y. Kivshar, H.-G. Park, *Nat. Commun.* **2021**, *12*, 4135.
[4] B. Zhen, C. W. Hsu, L. Lu, A. D. Stone, M. Soljacic, *Phys. Rev. Lett.* **2014**, *113*, 257401.
[5] H. M. Doeleman, F. Monticone, W. den Hollander, A. Alù, A. F. Koenderink, *Nat. Photonics* **2018**, *12*, 397.
[6] T. C. Tan, Y. K. Srivastava, R. T. Ako, W. Wang, M. Bhaskaran, S. Sriram, I. Al-Naib, E. Plum, R. Singh, *Adv. Mater.* **2021**, *33*, 2100836.
[7] C. Kyaw, R. Yahiaoui, J. A. Burrow, V. Tran, K. Keelen, W. Sims, E. C. Red, W. S. Rockward, M. A. Thomas, A. Sarangan, I. Agha, T. A. Searles, *Commun Phys* **2020**, *3*, 212.
[8] Z. Yu, X. Sun, *Light Sci Appl* **2020**, *9*, 1.
[9] M. Parry, A. Komar, B. Hopkins, S. Campione, S. Liu, A. E. Miroshnichenko, J. Nogan, M. B. Sinclair, I. Brener, D. N. Neshev, *Appl. Phys. Lett.* **2017**, *111*, 053102.
[10] A. Barreda, C. Zou, A. Sinelnik, E. Menshikov, I. Sinev, T. Pertsch, I. Staude, *Opt. Mater. Express* **2022**, *12*, 3132.
[11] E. Mikheeva, K. Koshelev, D.-Y. Choi, S. Kruk, J. Lumeau, R. Abdeddaim, I. Voznyuk, S. Enoch, Y. Kivshar, *Opt. Express* **2019**, *27*, 33847.
[12] Q. Wang, E. T. F. Rogers, B. Gholipour, C.-M. Wang, G. Yuan, J. Teng, N. I. Zheludev, *Nat. Photonics* **2015**, *10*, 60.
[13] J. Tian, H. Luo, Y. Yang, F. Ding, Y. Qu, D. Zhao, M. Qiu, S. I. Bozhevolnyi, *Nat. Commun.* **2019**, *10*, 396.
[14] Y. Wang, P. Landreman, D. Schoen, K. Okabe, A. Marshall, U. Celano, H.-S. P. Wong, J. Park, M. L. Brongersma, *Nat Nanotech* **2021**, *16*, 667.
[15] T. Driscoll, H.-T. Kim, B.-G. Chae, B.-J. Kim, Y.-W. Lee, N. M. Jokerst, S. Palit, D. R. Smith, M. Di Ventra, D. N. Basov, *Science* **2009**, *325*, 1518.
[16] S.-Q. Li, X. Xu, R. M. Veetil, V. Valuckas, R. Paniagua-Domínguez, A. I. Kuznetsov, *Science* **2019**, *364*, 1087.
[17] A. M. Shaltout, V. M. Shalaev, M. L. Brongersma, *Science* **2019**, *364*, eaat3100.
[18] X. Y. Chin, D. Cortecchia, J. Yin, A. Bruno, C. Soci, *Nat. Commun.* **2015**, *6*, 7383.
[19] G. Xing, N. Mathews, S. S. Lim, N. Yantara, X. Liu, D. Sabba, M. Gratzel, S. Mhaisalkar, T. C. Sum, *Nat. Mater.* **2014**, *13*, 476.
[20] S. Makarov, A. Furasova, E. Tiguntseva, A. Hemmetter, A. Berestennikov, A. Pushkarev, A. Zakhidov, Y. Kivshar, *Adv. Opt. Mater.* **2019**, *7*, 1800784.
[21] B. Gholipour, G. Adamo, D. Cortecchia, H. N. Krishnamoorthy, M. D. Birowosuto, N. I. Zheludev, C. Soci, *Adv. Mater.* **2017**, *29*, 1604268.
[22] Y. Fan, Y. Wang, N. Zhang, W. Sun, Y. Gao, C. W. Qiu, Q. Song, S. Xiao, *Nat. Commun.* **2019**, *10*, 2085.
[23] G. Adamo, H. N. Swaha Krishnamoorthy, D. Cortecchia, B. Chaudhary, V. Nalla, N. I. Zheludev, C. Soci, *Nano Lett.* **2020**, *20*, 7906.
[24] H. Zhu, Y. Fu, F. Meng, X. Wu, Z. Gong, Q. Ding, M. V. Gustafsson, M. T. Trinh, S. Jin, X. Y. Zhu, *Nat. Mater.* **2015**, *14*, 636.
[25] Y. Wang, X. Quintana, J. Kim, X. Guan, L. Hu, C.-H. Lin, B. T. Jones, W. Chen, X. Wen, H. Gao, T. Wu, *Photonics Research* **2020**, *8*, A56.
[26] S. Liu, S. Sun, C. K. Gan, A. G. Del Águila, Y. Fang, J. Xing, T. T. H. Do, T. J. White, H. Li, W. Huang, *Sci. Adv.* **2019**, *5*, eaav9445.
[27] Y. Jiang, A. M. Soufiani, A. Gentle, F. Huang, A. Ho-Baillie, M. A. Green, *Appl. Phys. Lett.* **2016**, 108.
[28] W. Kong, Z. Ye, Z. Qi, B. Zhang, M. Wang, A. Rahimi-Iman, H. Wu, *Phys. Chem. Chem. Phys.* **2015**, *17*, 16405.
[29] D. Cortecchia, S. Neutzner, J. Yin, T. Salim, A. R. Srimath Kandada, A. Bruno, Y. M. Lam, J. Martí-Rujas, A. Petrozza, C. Soci, *APL Mater.* **2018**, *6*, 114207.
[30] E. Y. Tiguntseva, Z. Sadrieva, B. V. Stroganov, Y. V. Kapitonov, F. Komissarenko, R. Haroldson, B. Balachandran, W. Hu, Q. Gu, A. A. Zakhidov, A. Bogdanov, S. V. Makarov, *Appl. Surf. Sci.* **2019**, *473*, 419.
[31] C. W. Hsu, B. Zhen, A. D. Stone, J. D. Joannopoulos, M. Soljačić, *Nat. Rev. Mater.* **2016**, *1*, 16048.
[32] T. Bauer, S. Orlov, U. Peschel, P. Banzer, G. Leuchs, *Nat. Photonics* **2013**, *8*, 23.
[33] Y. Zhang, J. Shen, C. Min, Y. Jin, Y. Jiang, J. Liu, S. Zhu, Y. Sheng, A. V. Zayats, X. Yuan, *Nano Lett.* **2018**, *18*, 5538.
[34] Q. Zhan, *Adv. Opt. Photonics* **2009**, *1*, 1.
[35] M. Xian, Y. Xu, X. Ouyang, Y. Cao, S. Lan, X. Li, *Sci. Bull.* **2020**, *65*, 2072.
[36] K. V. Sreekanth, S. Han, R. Singh, *Adv. Mater.* **2018**, *30*, 1706696.
[37] Z. Li, J. Moon, A. Gharajeh, R. Haroldson, R. Hawkins, W. Hu, A. Zakhidov, Q. Gu, *ACS Nano* **2018**, *12*, 10968.
[38] W. Liu, M. Li, R. S. Guzzon, E. J. Norberg, J. S. Parker, M. Lu, L. A. Coldren, J. Yao, *Nat. Commun.* **2017**, *8*, 15389.
[39] Q. Song, M. Odeh, J. Zúñiga-Pérez, B. Kanté, P. Genevet, *Science* **2021**, *373*, 1133.
[40] A. B. Khanikaev, G. Shvets, *Nat. Photonics* **2017**, *11*, 763.
[41] G. W. Burr, M. J. Breitwisch, M. Franceschini, D. Garetto, K. Gopalakrishnan, B. Jackson, B. Kurdi, C. Lam, L. A. Lastras, A. Padilla, *J. Vac. Sci. Technol., B: Nanotechnol. Microelectron.: Mater., Process., Meas., Phenom.* **2010**, *28*, 223.
[42] P. Whitfield, N. Herron, W. Guise, K. Page, Y. Cheng, I. Milas, M. Crawford, *Sci. Rep.* **2016**, *6*, 35685.
[43] I. Friedrich, V. Weidenhof, W. Njoroge, P. Franz, M. Wuttig, *J. Appl. Phys.* **2000**, *87*, 4130.